Pressure Drag of Obstacles in the Atmospheric Boundary Layer

STEFAN EMEIS

Institut für Meteorologie und Klimaforschung, Universität/Kernforschungszentrum Karlsruhe, Federal Republic of Germany

(Manuscript received 15 May 1989, in final form 27 November 1989)

ABSTRACT

Pressure drag of obstacles in the atmospheric boundary layer is computed with a mesoscale numerical model of the troposphere. Different parts of the drag can be separated from the numerical results: total pressure drag is determined from the surface pressure distribution, hydrostatic drag from the temperature distribution in the atmosphere, and form drag as a residual. The dependence of the different parts of the drag on the main influencing parameters, such as geometric parameters, dynamical and thermal parameters, and the surface roughness, is given. The influencing parameters are deduced from a scale analysis of the equation of motion. Wave drag due to gravity waves and flow separation will not be considered in this paper.

The study shows among other points that there is a surface Rossby number similarity for form drag on smooth obstacles, that there may be wave drag due to inertial waves even for neutral or unstable stratification due to inertial waves, and that there is Reynolds number similarity for form drag only with respect to molecular viscosity and not with respect to turbulent viscosity of the air. The results suggest the separation of form drag into two parts: a viscous form drag due to turbulent viscosity of the air, and a turbulent form drag due to additional production of turbulence in the vicinity (mainly in the lee) of the obstacle. The distinction of different drag producing mechanisms will help in the task of parameterization.

Parameterization using similarity theories is meaningful only for ensembles of obstacles. Here, isolated obstacles are considered for simplicity, therefore, only the prerequisites for the parameterization are discussed in this paper. The main result is that parameterization of pressure drag in terms of an effective roughness length using Rossby number similarity theory will be possible only for the two parts of the form drag. All other parts of the drag have no corresponding mechanisms in the homogenous boundary layer.

1. Introduction

a. Previous work

Pressure drag (mountain drag) is one of the two sinks in the atmospheric momentum budget. If this drag is a subgridscale phenomenon in a numerical model (this depends on the horizontal scale of the model) it has to be parameterized. In order to do this the dependence of the drag on gridscale parameters must be known. In a recent paper (Emeis 1987, called E87 hereafter) the author has computed with a numerical model the pressure drag with neutral stratification over complex terrain and presented an attempt to express this drag by means of an effective roughness length. In order to compare these results to experimental studies the length scale L of the obstacles had been chosen in the order of the boundary layer height δ, and the roughness length z_0 on the surface of the obstacles was kept fixed at a rather high value typical for an area partly covered by trees and forests. Furthermore, the shape of the obstacles was sinusoidal and symmetrical. Under these assumptions the height H of the obstacles and their spatial density $1/D$ were varied. Using the resistance law of the Rossby number similarity theory a parameterization of the effective roughness length was found depending only on the mean slope H/L of the terrain and the initial roughness length z_0. The parameterization was valid for closely spaced sinusoidal obstacles with small to moderate slopes ($H/L \leq 0.2$) and fit quite well to some observations over complex terrain.

The main input for this parameterization was the dependence of the pressure drag on the mean slope H/L of a single sinusoidal obstacle computed with a two-dimensional numerical model. But there are other parameters that influence the drag on such an obstacle too. Remembering the results of Nikuradse and Prandtl (see Prandtl et al. 1984) of measurements of the drag on smooth and rough plates and in pipes in a turbulent flow, the drag coefficient should depend on the Reynolds number (decrease with increasing Re) and on the surface roughness (increase with increasing z_0) as long as the obstacle surface can be considered aerodynamically rough. For smooth plates and pipes the drag depends only on the Reynolds number. This is equivalent to the statement made by the Rossby number similarity theory for the homogeneous boundary layer that for small roughness lengths (i.e., high Rossby numbers formed with the surface roughness length z_0) the drag coefficient does not depend on the Rossby number.

Corresponding author address: Dr. Stefan Emeis, Institut für Meteorologie und Klimaforschung, Universität Karlsruhe (TH), Kaiserstrasse 12, D-7500 Karlsruhe 1, Federal Republic of Germany.

Varying the Reynolds number to smaller values than in E87, a problem will be encountered if the geostrophic wind is used as a scaling velocity. This scaling velocity is desirable because it is an external parameter that can easily be determined in larger-scale models when parameterizing drag over inhomogeneous terrain as a subgridscale phenomenon. The drag is proportional to about the square of the incident velocity. As an incident velocity the velocity at the height L above ground in the undisturbed flow upstream has to be taken (Jackson and Hunt 1975). The height L had been found by Jackson and Hunt using analytical considerations. It takes into account the vertical shear of boundary layer flow. This is the reason why the ratio L/δ (δ is the height of the boundary layer) becomes important here. If L/δ is greater than unity the scaling velocity is always the geostrophic wind (which is assumed to be vertically constant for simplicity in the numerical model). For L/δ smaller than unity the scaling velocity is from inside the boundary layer and thus nearly always smaller than the geostrophic wind. Therefore, the drag coefficient formed with the geostrophic wind will decrease more and more, the shorter the length scale of the obstacle.

Simulations of the drag at much higher Reynolds numbers than in E87 incorporate another parameter that has been neglected so far, the Coriolis parameter f. For increasing Reynolds numbers the Rossby number formed with the length scale of the obstacle decreases. If the Rossby number is below the order of unity (neglecting a factor π), waves can be generated even under neutral stratification. These are inertial waves that produce a wave drag in addition to the form drag considered up to this point.

This wave drag is not in contradiction to the findings of Smith (1979) who found a lift force acting perpendicular to the direction of the geostrophic flow at elongated mountains but no drag. Because his calculations were made under the assumption of quasi-geostrophy ($L \ll u_g/f$) on a f-plane, there was no disturbance of the pressure field due to the presence of the mountain and no inertial waves were excited. Waves and a respective wave drag were produced only when he introduced a β-plane. The present numerical model is not quasi-geostrophic, so we have a pressure perturbation and a wave drag due to inertial waves also on the f-plane.

Neutral stratification has been considered thus far. Thus the drag discussed so far has been (with the exception of the inertial waves) pure form drag due to the production of turbulence in the direct vicinity of the obstacle and the viscosity of the air. Generally the atmosphere will be stratified, so the dependence of the drag on the stratification has to be taken into account. This may be easy for small deviations from neutral stability and small obstacles. But for stronger stable stratifications and larger obstacles things become much more complicated. The drag will then be composed out of three contributions: the form drag that will be the main topic in the following, the wave drag due to gravity waves (that is fairly well understood from linear and nonlinear analytic and numerical models, at least for homogeneously stratified media with no shear and no wavebreaking), and a hydrostatic drag that is due to the blockage of colder air by the obstacle.

The term hydrostatic in this context should not be mixed with the term hydrostatic in the approximation of the Navier–Stokes equations. We use a nonhydrostatic numerical model here, and hydrostatic means that this drag contribution is determined only from the temperature distribution across the obstacle. Following the five drag mechanisms (a to e) of Smith (1978), form drag corresponds to mechanism a, wave drag to b and c, and hydrostatic drag to d. Smith's mechanism e is not considered here.

Measurements of the total pressure drag of the Alps for different synoptic situations are reported in Hafner and Smith (1985). A list of various drag measurements on different mountains and a list of several theoretical and laboratory studies of the different drag mechanisms can be found in Davies and Phillips (1985). They found from ALPEX-SOP data (from March to April 1982) over the Alps along the Gotthard cross section that blockage of colder air on the upstream side was the prevalent drag mechanism and that wave drag was only a sporadically significant contributor to the drag during that period. Also Hafner (1987) made a decomposition of the total drag into several components from ALPEX-data and found that wave drag is more than one magnitude smaller than the total drag from the surface pressure distribution.

Shao and Hantel (1986) computed from budget studies vertical subsynoptic (i.e., subgridscale with respect $\Delta x = \Delta y = 63.5$ km, $\Delta p = 200$ hPa and $\Delta t = 1$ d) momentum fluxes in the troposphere and lower stratosphere over Europe for ALPEX-SOP. They found no signal caused by the Alps in the upper troposphere (400 hPa). This fits in the just mentioned results from Davies and Phillips that blockage of colder air was more important than the generation of lee waves. The blockage effect is not connected to a vertical momentum flux in the free atmosphere and therefore cannot be detected from upper-tropospheric data.

b. Scope of this paper

The determination of the different parts of the pressure drag in this paper is designed as follows: First, the main influencing nondimensional parameters which govern the different components of the total pressure drag are deduced from a scale analysis of the equation of motion. Then the numerical model is used to check the validity of the scaling assumptions to include nonlinear processes in the drag production that do not follow from the scale analysis, such as surface friction, flow separation, and blocking, and to compute the magnitude of the different parts of the drag. With the

numerical results each of the different drag components is described in terms of one or a combination of some of the nondimensional parameters arrived at from the scale analysis of the equation of motion. This description is a prerequisite for the parameterization of pressure drag in larger-scale models.

The same numerical model as in E87 will be used to investigate the aforementioned problems; it is a two-dimensional nonhydrostatic mesoscale numerical model of the troposphere with special resolution of the boundary layer and a first-order turbulence closure (Dorwarth 1986). From the output of the model after the simulation has become more or less stationary, it is possible to distinguish between the different parts of the drag. The total pressure drag is computed from the surface pressure distribution, the wave drag due to gravity waves from the velocity correlations aloft, and the hydrostatic drag from the temperature distribution. The form drag with stable stratification can then be determined as a residual.

The model is two-dimensional. Introducing a third dimension will not add any new drag producing mechanisms to those already present with two dimensions. But it is likely to change the magnitude of the different drag components. This will especially effect the blocking of colder air that is assumed to be reduced considerably if the flow can deviate horizontally and is not forced to cross over the obstacle completely. For the sake of simplicity and in order to keep the computational effort reasonable we use two dimensions. A study by Smith (1989) shows that if the ratio of the length scale perpendicular to the incident flow, to the length in the direction of the flow is larger than about 5 then the types of flow are nearly independent from this ratio. Therefore our results can be applied to obstacles where this ratio is greater than 5.

This study deals with obstacles smaller than the Alps ($L = 10^2$ to 10^4 m), but for these scales no experimental data on the different drag mechanisms are known to the author. The aim is to clarify the nature of the different parts of the drag, to study their dependence on external parameters, and to show which parts are important for mesoscale obstacles. This paper will concentrate on neutral stratification and small deviations from neutral stratification without flow separation. "Small" in this context will mean that the stratification will not be that strong for a given length of the obstacles that vertical propagating gravity waves form.

Obstacles with a length scale of about 10^2 m are too short to produce any gravity wave pattern under typical atmospherically stable stratifications. This is one reason why we exclude gravity wave drag here. Also, different parts of the drag cannot be decomposed linearly, as is done in this study, if wave pattern is present. Gravity wave drag, and its influence on the other parts of the total pressure drag, will be the subject of a separate paper (Emeis 1990).

Section 2 derives the different parts of pressure drag from a scale analysis of the equation of motion and introduces the influencing nondimensional parameters. Section 3 describes the numerical model and shows how the different parts of the drag are computed from the numerical results. Sections 4 and 5 present numerically calculated values for the pressure drag. Section 4 deals with neutral stability and section 5 with small deviations from this stability. The numerical results are displayed as functions of the nondimensional parameters introduced in section 2. The parameterization issue is addressed in section 6 followed by the conclusions in section 7.

2. Scale analysis of pressure drag

Total pressure drag is computed from the surface pressure distribution on the obstacle contour:

$$W_D = \frac{1}{2L}\int_{-\infty}^{\infty} p(x, z)\frac{dh}{dx}\,dx = \frac{1}{2L}\int\int \frac{\partial p}{\partial x}\,dxdz. \tag{1}$$

Here, $h(x)$ is the topography, L is half of the width of the obstacle, and $p(x, z)$ is the deviation of the pressure from a basic state without obstacle. The double integral on the right is taken over the whole $2D$ domain. The drag is normalized with the length of the sloped terrain $2L$.

From the horizontal equation of motion we get for stationarity:

$$\int\int \frac{\partial p}{\partial x}\,dxdz = -\int \rho uwdx - \int \rho u'w'dx + \int\int \rho fvdxdz + \int\int\int \rho \frac{\partial f}{\partial y}\,vdxdydz. \tag{2}$$

Here u, v, and w are deviations of the wind components due to the presence of the obstacle from the basic state without obstacle; u' and w' are fluctuations due to subgridscale, turbulent motions. The last term appears only if a β-plane is introduced ($\beta = \partial f/\partial y$). The first two terms on the right-hand side emerge from the vertical advection. Horizontal advection has been neglected because we are interested in the vertical transport of momentum down to the surface, and because we assume that the effects of the obstacle on the flow have vanished at the domain boundaries.

The variables are nondimensionalized using the horizontal and vertical length scales L and H of the obstacle and three velocity scales (incident motion: U, a turbulent velocity scale: $2.466 \cdot (\nu_t U^2/L)^{1/3}$, and a buoyant velocity scale: $\sigma^{1/2}L$). Each velocity is multiplied by H/L in order to have only the contribution that is due to the presence of the obstacle.

$$u = UH/Lu^* \qquad u' = 2.466(\nu_t U^2/L)^{1/3}H/Lu'^*$$
$$v = UH/Lv^* \qquad w' = 2.466(\nu_t U^2/L)^{1/3}H/Lw'^*$$
$$w = \sigma^{1/2}LH/Lw^* \qquad p = \rho U^2 H/Lp^*$$
$$x = Lx^*$$
$$y = Ly^*$$
$$z = Hz^*$$

The star denotes nondimensional quantities; σ is a stability parameter ($=g/\theta \cdot \partial\theta/\partial z$). The bouyant velocity scale makes sense only for stable conditions, then $\sigma = N^2$ (N is the Brunt–Väisälä frequency), and θ is potential temperature.

Here, ν_t is a turbulent viscosity introduced in analogy to the molecular viscosity. In contrast to the molecular viscosity which is a property of the fluid, the turbulent viscosity is a field variable that describes the interaction between different layers of the fluid due to turbulent velocity fluctuations. Therefore, ν_t is not an external variable, and a scaling using this variable becomes a local scaling. In order to return to external variables, which is necessary for a parameterization scheme for larger-scale models, ν_t has been kept constant ($=5\ m^2\ s^{-1}$) when it is used as a scaling parameter. The value has been chosen as a mean value of the exchange coefficient computed by the numerical model for the flow domain. The numerical results will show that this procedure is justified in principle. With a constant ν_t we now have a complete analogy to the molecular viscosity.

The turbulent velocity scale comes from dimensional arguments. The pressure drag due to turbulent fluctuations arises when an obstacle of length L has to be passed. The deformation of the velocity field necessary for this passing over is counteracted by the turbulent viscosity. This results in dissipation ϵ. We put for the turbulent velocity fluctuations

$$u' = \epsilon^{1/3}L^{1/3}. \tag{3}$$

The most simple process of dissipation is isotropic turbulent dissipation which can be written as

$$\epsilon = 15\nu_t\left(\frac{\partial u}{\partial x}\right)^2. \tag{4}$$

Dimensional arguments lead to

$$\epsilon = 15\nu_t\frac{U^2}{L^2}. \tag{5}$$

Putting this into the expression for u' results in the velocity scale for the turbulent fluctuations:

$$u' = 2.466 \cdot \nu_t^{1/3}U^{2/3}L^{-1/3}. \tag{6}$$

Defining a nondimensional stability parameter $\sigma^{*1/2} = \sigma^{1/2}L/U$, an obstacle Rossby number $\mathrm{Ro}_o = U/fL$, a planetary Rossby number $\mathrm{Ro}_p = U/\beta L^2$, and a turbulent Reynolds number $\mathrm{Re}_t = UL/\nu_t$ [Tennekes (1973) calls it a Townsend number] we get for the pressure drag

$$W_D = \frac{1}{2}\rho U^2\frac{H^2}{L^2}\left(-\sigma^{*1/2}\int u^*w^*dx^* - \frac{6.082}{\mathrm{Re}_t^{2/3}}\int u'^*w'^*dx^* + \frac{1}{\mathrm{Ro}_o}\iint v^*dx^*dz^* + \frac{1}{\mathrm{Ro}_p}\iiint v^*dx^*dy^*dz^*\right). \tag{7}$$

Forming a drag coefficient by normalizing with the kinetic energy of the incident velocity yields

$$C_W = \frac{H^2}{L^2}\left(-\sigma^{*1/2}\int u^*w^*dx^* - \frac{6.082}{\mathrm{Re}_t^{2/3}}\int u'^*w'^*dx^* + \frac{1}{\mathrm{Ro}_o}\iint v^*dx^*dz^* + \frac{1}{\mathrm{Ro}_p}\iiint v^*dx^*dy^*dz^*\right). \tag{8}$$

The term with $\sigma^{*1/2}$ is present only if we have waves that transport momentum downward. For neutral stability and no rotation (8) reduces to

$$C_{WN} = -\frac{H^2}{L^2}\frac{6.082}{\mathrm{Re}_t^{2/3}}\int u'^*w'^*dx^*. \tag{8a}$$

For stably stratified, irrotational, inviscid flow using $\sigma^{*1/2} = \mathrm{Fr}$ (Froude number) we get:

$$C_{WS} = -\frac{H^2}{L^2}\int u^*w^*dx^* \tag{8b}$$

which equals the linear solution for hydrostatic irrotational mountain waves if the integral turns out to be $-\pi/2$. Wave drag has been kept in this scaling analysis for the sake of completeness but it is not considered further in this paper.

The third term on the right-hand side of (8) describes the effect of inertial waves and the last term planetary Rossby waves. Not included in this linear approach (i.e., that the different parts of the drag, so far, can be decoupled from each other) is the blockage of colder air masses by an obstacle (this would violate the condition that effects of the obstacle vanish far away from the obstacle) and the production of additional turbulence in the direct vicinity of the obstacle if the surface of the obstacle is aerodynamically rough (this could not be separated from the viscous form-drag by scale analysis). These processes introduce a second Froude number $\mathrm{Fr}_h = NH/U$ and a surface Rossby number $\mathrm{Ro}_s = U/fz_0$, respectively. Additional turbulence

means turbulence that is produced by the presence of the obstacle in addition to the subgridscale turbulence (in terms of the used numerical model, see section 3) in the homogeneous boundary layer of the incident flow. This may be subgridscale turbulence again, which is formed in the layer close to the obstacle contour and in the lee of the obstacle (this turbulence is handled by the turbulence closure scheme of the numerical model and is mainly due to the surface roughness and the increased wind shear over the obstacle), or gridscale turbulence, which is resolved by the numerical model in the form of a separation bubble in the lee of the obstacle. The latter is not (with the exception of section 4a) considered in this study.

Thus the drag coefficient C_W can be regarded as a function of seven main parameters:

$$C_W = f\left(\frac{H}{L}, \mathrm{Re}_t, \sigma^*, \mathrm{Fr}_h, \mathrm{Ro}_o, \mathrm{Ro}_s, \mathrm{Ro}_p\right). \quad (9)$$

The length and height scales L and H are defined by the shape of the sinusoidal obstacle:

$$h(x) = \begin{cases} \dfrac{H}{2}\left(\sin\left(\dfrac{|x - x_m|}{L} + \dfrac{1}{2}\right)\pi + 1\right) \\ \qquad \text{for} \quad \dfrac{|x - x_m|}{L} \leq 1 \\ 0 \quad \text{for} \quad \dfrac{|x - x_m|}{L} > 1 \end{cases} \quad (10)$$

where L is half of the width of the obstacle and H is the crest height.

For the velocity scale U, as mentioned already in the Introduction, two choices are possible. Using the external parameter u_g introduces the boundary layer height δ (for the homogeneous boundary layer we have $\delta = \kappa u_*/f$, where κ is von Kármán's constant and u_* is a function of z_0 and u_g from the Rossby number similarity theory) as an additional parameter. Here, δ will be normalized with the length scale L. Inserting in (8) yield

$$C_W^{(1)} = \frac{W_D}{\frac{1}{2}\rho u_g^2} = f^{(1)}\left(\frac{H}{L}, \mathrm{Re}_t, \sigma^*, \mathrm{Fr}_h, \mathrm{Ro}_o, \mathrm{Ro}_s, \mathrm{Ro}_p, \frac{\delta}{L}\right). \quad (11)$$

The other possibility is to use the internal parameter $u(z = \alpha \cdot L)$, which is the scaling velocity for the inner layer in two-layer and three-layer analytical models (e.g., Jackson and Hunt 1975). The present numerical simulations with sinusoidal obstacles have shown that the influence of the boundary layer height δ is removed almost completely if α is chosen to equal 0.3. Inserting this velocity scale in (8) defines

$$C_W^{(2)} = \frac{W_D}{\frac{1}{2}\rho u^2(0.3L)} = f^{(2)}\left(\frac{H}{L}, \mathrm{Re}_t, \sigma^*, \mathrm{Fr}_h, \mathrm{Ro}_o, \mathrm{Ro}_s, \mathrm{Ro}_p\right). \quad (12)$$

The parameters Re_t, Ro_o, Ro_s, Ro_p, $\sigma^{*1/2}$ and Fr_h will all be formed with $U = u_g$. The length scale will be chosen short enough that Ro_o is larger than 1 and Ro_p is much larger than 1.

3. Numerical model

The two-dimensional version of the mesoscale numerical model KAMM (Karlsruhe atmospheric mesoscale model) developed at the Institut für Meteorologie und Klimaforschung has been used for this study. The model is a prognostic, nonhydrostatic, primitive-equation gridpoint-model with a constant horizontal and a variable vertical gridwidth (Dorwarth 1986; Emeis 1987). In the following the vertical gridwidth varies from 14 m in the lower boundary layer to some hundred meters in the upper troposphere, and the horizontal gridwidth is between 500 and 10 000 m. The length of the time step is controlled by the model in order to obey the CFL-criterion. It is usually between 3 and 10 seconds. The number of gridpoints is 122 and 30 in the horizontal and vertical directions respectively. The height of the model domain is 8000 m.

Turbulence closure is done by computing an exchange coefficient from a two-equation model for eddy viscosity (Mellor and Yamada 1982). There are two equations, one for the turbulent kinetic energy and one for the mixing length. The latter had been changed from a diagnostic to a prognostic equation by Dorwarth (1986). This turbulence model is a "first-order closure."

Boundary conditions are a no-slip condition at the lower boundary, which is identical to the topography (the coordinate system follows topography), radiation conditions at the lateral boundaries, and a damping layer at the top of the model domain. Sound waves are filtered out by forcing the wind field free of divergences.

The model is driven by an external force on the synoptic scale. This force is represented by a prescribed geostrophic wind in the whole model domain. The geostrophic wind is vertically constant in this study, so we simulate a barotropic atmosphere. The geostrophic wind is always perpendicular to the obstacle which is assumed to be indefinitely long in the cross-wind direction.

The model computes nonhydrostatic deviations from a hydrostatic horizontally homogeneous initial state without an obstacle (basic state). The initial state

is given by a one-dimensional model with identical physics, and is defined by the geostrophic wind, the vertical temperature profile, the surface roughness, the surface temperature, and the height of the model domain.

A flow with stable stratification is initialized with a stable one-dimensional temperature profile and a surface temperature that fits into the vertical temperature gradient in order to have near-zero surface heat flux. The stability is constant in the vertical. A flow with unstable thermal conditions is initialized with a neutral temperature profile and a surface temperature that is higher than the air temperature near the ground. From this initial state an unstable temperature profile in the two-dimensional model forms during the simulation. So we have no inversion at the top of the unstable boundary layer. The temperature gradient in the lower boundary layer (a few times the height of the obstacle) at the end of the simulation is then used, forming the parameter that describes the thermal stratification σ.

The two-dimensional model with topography is iterated until the solution becomes stationary. The pressure, wind, and temperature fields from this stationary solution are then used to compute the pressure drag and its components. For neutral stratification and mesoscale obstacles where the Coriolis force in unimportant, a stable solution is reached after 2 to 4 hours of simulation time. For nonneutral stratifications a stable solutions cannot be expected a priori because the model always looses or gains energy at the surface. Despite this we have found a more or less stable solution after a few hours (at least 4) from which we took the fields necessary to compute the drag. We think that the usage of this "quasistationarity" is justified because in real nature the external forces and conditions are never exactly constant for longer periods.

The shape of the obstacle had already be defined in (10). It was always situated in the center of the two-dimensional domain. Each slope of the obstacle was represented by at least 5 gridpoints in x-direction, and each lateral boundary of the model domain was at least 5 times half of the width of the obstacle away from the foot of the obstacle.

The total pressure drag is computed from (1). For the computation of the hydrostatic pressure drag due to the blockage of colder air masses at the upwind side of the obstacle, a hydrostatic surface pressure deviation is found by vertical integration of the deviation of the temperature from the basic state. This pressure deviation is then inserted into (1) to yield the hydrostatic part of the total pressure drag. The form drag and the wave drag due to inertial waves are found as a residual from the total pressure drag and the hydrostatic pressure drag. This linear decomposition is thought to be valid as long as no waves occur. The nonlinear interaction between form drag and wave drag and between hydrostatic drag and wave drag will be dealt with in another paper (Emeis 1990).

4. Numerical results for neutral stratification

a. Dependence of the drag on the geometric parameter H/L

For neutral conditions, neglecting Ro_p, we should have from (12)

$$C_{W\,\mathrm{neutral}}^{(2)} = f_{\mathrm{neutral}}^{(2)}\left(\frac{H}{L}, \mathrm{Re}_t, \mathrm{Ro}_o, \mathrm{Ro}_s\right). \quad (13)$$

The dependence of the drag on H/L for neutral conditions, no rotation, $\mathrm{Re}_t \approx 5 \cdot 10^3$, $\mathrm{Ro}_s \approx 2 \cdot 10^5$, and $L/\delta \approx 2$ was presented in E87. The main result was the drag coefficient for a single sinusoidal mountain ($0.01 < H/L \approx 0.6$):

$$C_{W0}^{(1)} = 0.358\left(\frac{H}{L}\right)^{2.17}, \quad (14)$$

and a similar expression for a single valley ($H < 0$). Equation (14) also includes cases with flow separation. For $H/L \geq 0.3$ flow separation sets in and the drag is enhanced due to the production of the wake circulation. Therefore, the dependence of $C_{W0}^{(1)}$ on H/L is somewhat larger than with the second power. For small H/L with no flow separation, $C_{W0}^{(1)}$ could be written as $\approx 0.2 \cdot (H/L)^2$, now having the squared dependence on the slope, as expected from (8a). Here, $6.082/\mathrm{Re}_t^{2/3}$ is about 0.02 which means that the integral over the dimensionless wind fluctuations in (8a) has to come out at about 10, which is one order of magnitude too large for a term containing only quantities scaled to an order of one. This indicates that the scaling is not completely correct. We will come back to this point at the end of section 4b.

The drag coefficient for closely spaced sinusoidal obstacles ($0.1 \approx H/L \approx 0.3$) was found to be

$$C_W{}^{(1)} = 0.074\left(\frac{H}{L}\right)^{1.48}. \quad (15)$$

Here, there is no longer any difference between mountains and valleys. This result was the basis for the estimation of the effective roughness length $z_{0\mathrm{eff}}$:

$$\ln\left(\frac{z_{0\mathrm{eff}}}{z_0}\right) = 20\,\frac{H}{L}. \quad (16)$$

Assuming that the dependence of $C_W{}^{(i)}$, $i = 1, 2$ on H/L is independent of the other parameters (a statement that can only be proven by experiments) we can normalize $C_W{}^{(i)}$ with C_{W0}:

$$C_{WR}^{(i)} = \frac{C_W{}^{(i)}}{C_{W0}}, \quad i = 1, 2. \quad (17)$$

b. Dependence of the drag on the length scale and the surface roughness

As already discussed in the introduction the effective roughness length in E87 had been derived for a fixed

length scale L in the order of the boundary layer height δ. In order to find the dependence of the drag on Re_t, Ro_o, and Ro_s, the length scale L and the roughness length z_0 (this also leads to a variation of the boundary layer height δ) have been varied in the following, keeping the slope H/L constant and the stratification neutral.

A typical result is presented in Fig. 1. For $H/L = 0.1$ the normalized drag coefficient $C_{WR}^{(1)}$ from (17) is plotted here against the logarithms of the obstacle Rossby number Ro_o and the surface Rossby number Ro_s.

This plot can be divided into several parts bounded by two nearly vertical and one horizontal line. The nearly vertical line to the right is the line $L/\delta = 0.9$ that separates small obstacles inside the boundary layer (region C) and larger obstacles whose influence reaches higher up than the boundary layer height (region B). The nearly vertical line to the left separates the larger mountains from those where the Coriolis force is important to the flow and the resulting drag, (region A) and those where the Coriolis force is negligible (region B). The horizontal line at about $Ro_s = 5 \times 10^5$ divides smooth (subregion 1) and rough obstacles (subregion 2) from each other.

It was already mentioned in the Introduction that principally we want to keep the geostrophic wind as a scaling parameter because it is an external parameter. But the effects of the surface roughness and the Coriolis force on the drag can be made clearer by skipping this demand. Therefore, Fig. 2 shows $C_{WR}^{(2)}$.

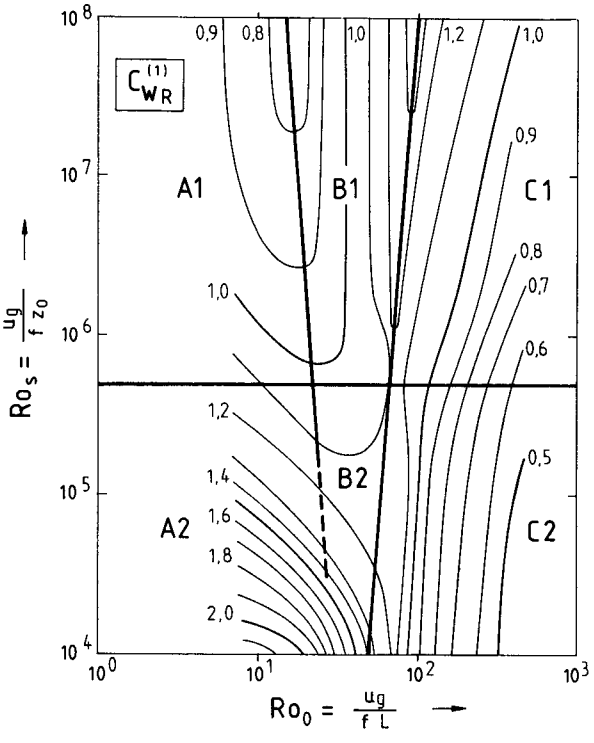

FIG. 1. Drag coefficient $C_{WR}^{(1)}$ [see (11) and (17)] for slope $H/L = 0.1$ as function of obstacle Rossby number and surface Rossby number from numerical simulations. Thick lines separate different regions A1, B1, ... (see text).

Now the line $L/\delta = 0.9$ is no longer of any importance and the figure is divided in four subregions only. In region B the Coriolis force has no effect on the drag whereas in region A the rotation of the earth is important. Again a horizontal line at $Ro_s = 5 \times 10^5$ is separating smooth and rough obstacles. From the numerical results it seems that for rough obstacles the line between the subregions A2 and B2 is vertical (constant $Ro_o = 3 \times 10^{-2}$), but that for smooth obstacles the trough line of minimal drag is slightly dependent on the surface roughness length. This fact will be looked at again when discussing the role of the Coriolis force further below.

We will start the physical explanation of Fig. 2 with subregion B1. In this region the obstacle has a smooth surface, the surface roughness had no influence on the magnitude of the drag, and no additional turbulence is produced in the direct vicinity of the obstacle. The Coriolis force is negligible here and therefore the drag cannot depend on the obstacle Rossby number Ro_o. But we still find a variation with Ro_o. As u_g is constant and f is unimportant here this is a varition with $1/L$. The remaining drag mechanism that varies with length scale L is the term due to the viscosity of the air streaming over the obstacle. As the usual Reynolds number formed with the length scale L and the *molecular* viscosity is clearly beyond the critical value for the transition to turbulence, the airflow over the obstacle is a turbulent flow and thus cannot depend on this Reynolds number. Therefore, the drag must be proportional to the *turbulent* viscosity of the air and to the displacement of the flow by the obstacle. It is not the slope of the obstacle contour but its curvature that is important to the displacement. For fixed slope the curvature decreases with increasing length scale L.

Thus the drag decreases with increasing *turbulent* Reynolds number Re_t. We will find the influence of the turbulent viscosity again in section 5 when we introduce stratification.

By a simple consideration it is shown that pure turbulent viscosity without surface friction can produce drag. The most ideal type of flow over an obstacle is potential streamflow that produces no drag. The surface pressure distribution is characterized by a pressure minimum exactly over the crest of the obstacle. For a symmetric obstacle the pressure distribution is also symmetric to the crest line, so that Eq. (1) always gives exactly zero. Potential flow theory assumes that the air has no viscosity. Introducing viscosity now (a turbulent viscosity in our case represented by turbulent velocity fluctuations $u_i'^2$) changes the surface pressure distribution. It is assumed that the incident turbulent airflow upstream of the obstacle is in equilibrium with the surface having turbulent velocity fluctuations $u_{i0}'^2$.When

this airflow hits the obstacle the flow is forced to be vertically convergent over the upwind slope and vertically divergent over the downwind slope of the obstacle. On the other hand, convergence suppresses turbulence and divergence supports turbulence, i.e.

$$\begin{cases} u_3'^2 - u_{3_0}'^2 < 0 & \text{for } \dfrac{dh}{dx} > 0 \\ u_3'^2 - u_{3_0}'^2 > 0 & \text{for } \dfrac{dh}{dx} < 0. \end{cases} \tag{18}$$

For the pressure distribution on the surface in a turbulent flow the following relation holds (Prandtl et al. 1984, p. 195):

$$\frac{\partial \bar{p}}{\partial x} = \frac{\partial \overline{p_0}}{\partial x} - \rho \frac{\partial \overline{w'^2}}{\partial x} \tag{19}$$

where $\overline{p_0}$ is the pressure at the surface or in boundary layers at the edge of the turbulent zone and $w'^2 = u_3'^2$.

This implies that surface pressure increases from the value of potential flow theory on the upwind slope of the obstacle and decreases on the downwind slope leading to a resulting pressure drag. The pressure minimum is shifted towards the leeward slope.

This consideration again leads to the conclusion that the pressure drag should be proportional to $(H/L)^2$ as shown in (8). With the pressure having a component proportional to the slope [(18) and (19)] the integral in (1) is proportional to the square of the slope.

The aforementioned process has been proven by analytical calculations by Sykes (1980). He presented a triple-layer model for the flow over a gentle hill. In the outer layer he introduced turbulent viscosity with a second-order closure. As this outer layer does not feel the surface roughness this calculation can be compared to the situation in subregion B1 in Fig. 2. He also found an asymmetric pressure distribution for a symmetrical obstacle at the lower boundary of the outer layer and a resulting pressure drag proportional to the square of the slope.

In summary, the drag coefficient $C_W^{(2)}$ in subregion B1 on a smooth single obstacle in neutral stratification depends only on H/L and Re_t and does not depend on Ro_s. This behavior corresponds to the Rossby number similarity of the homogeneous boundary layer where the drag coefficient becomes independent of the surface roughness for large values of the Rossby number.

There is a fixed relation between Re_t and Ro_o if u_g, f, and ν_t are kept constant as done in this paper:

$$\mathrm{Re}_t = \frac{u_g^2}{\nu_t f} \frac{1}{\mathrm{Ro}_o} = 144\,500 \frac{1}{\mathrm{Ro}_o}. \tag{20}$$

Neglecting the term with Ro_p, from (8) neutral conditions are,

$$C_{W\,\text{neutral}}^{(2)} = \frac{H^2}{L^2}\left(-\frac{6.082}{\mathrm{Re}_t^{2/3}}\int u'^*w'^*dx^* + \frac{1}{\mathrm{Ro}_o}\int\int v^*dx^*dz\right). \tag{21}$$

Inserting (20) into this expression yields

$$C_{W\,\text{neutral}}^{(2)} = \frac{H^2}{L^2}\left(-\frac{6.082}{\mathrm{Re}_t^{2/3}}\int u'^*w'^*dx^* + \frac{\mathrm{Re}_t}{144\,500}\int\int v^*dx^*dz^*\right). \tag{22}$$

This shows that the drag coefficient for neutral conditions, no flow separation, and aerodynamically smooth obstacles (no influence of Ro_s) can be written as a function of H/L and Re_t only.

Figure 3 displays the drag coefficient $C_W^{(2)}$ from (13) versus the turbulent Reynolds number. The parameters varied in Fig. 3 are the surface roughness (solid lines) and the Coriolis parameter (broken lines). Thus the solid lines are cross sections through Fig. 2 for constant Ro_s. Figure 3 is plotted for $H/L = 10^{-2}$ but shows the same structural behavior as Fig. 2. This is to show that the effects discussed here do not depend on the slope of the obstacle (at least when no flow separation takes place).

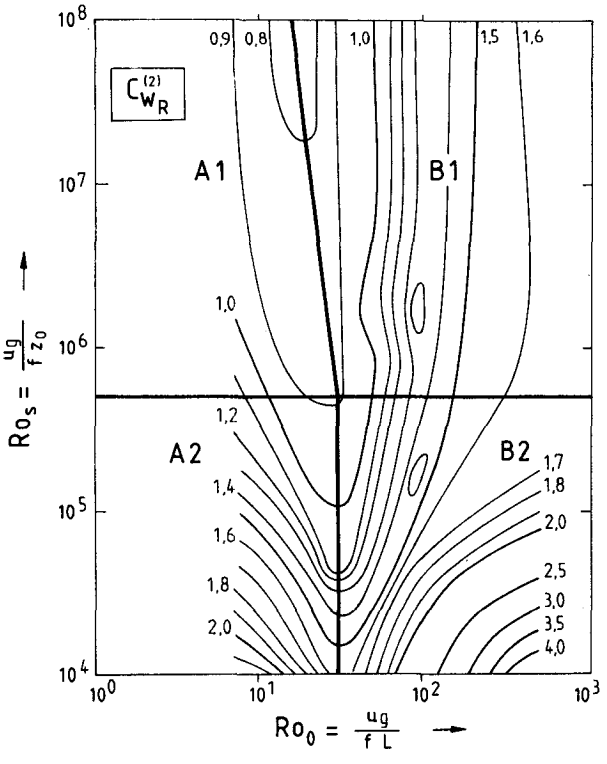

FIG. 2. As Fig. 1, but for drag coefficient $C_{WR}^{(2)}$, see (12) and (17).

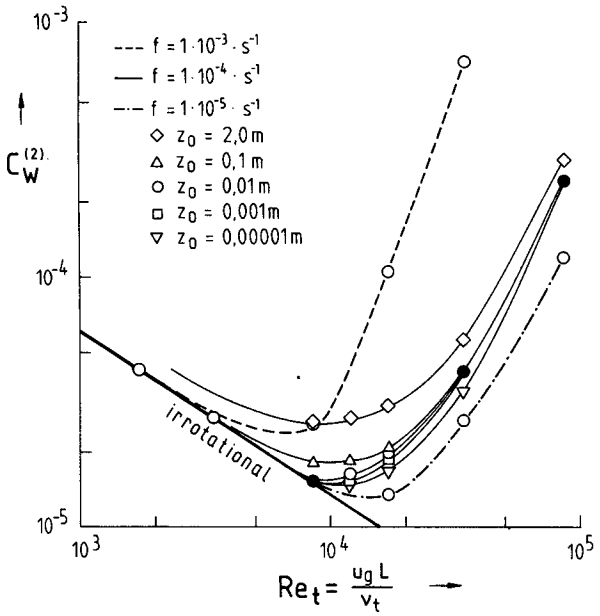

FIG. 3. Drag coefficient $C_W^{(2)}$ for slope $H/L = 0.01$ as function of turbulent Reynolds number. The plot is valid for different surface Rossby numbers (open symbols for different roughness lengths, full circles indicate that more than two symbols fall together) and for different values of the Coriolis parameter f.

Figure 3 reminds one of the well-known figures of Nikuradse and Prandtl (see Prandtl et al. 1984). There the drag on a plate also decreased with increasing Reynolds number in a turbulent flow and increased with increasing surface roughness. These features are prominent here again, with the only exception that with increasing length scale L the drag is finally rising again. This is due to inertial gravity waves that are excited by the obstacle. Thus we find a wave drag with neutral stratification.

This fact is elucidated in Fig. 4, which shows the dispersion relation of vertical wavenumber l of vertically propagating waves that depend on the stability parameter σ, the incident flow speed U, and the horizontal wave number k of the obstacle:

$$l^2 = \frac{\sigma - k^2U^2}{k^2U^2 - f^2}\,k^2; \tag{23}$$

see e.g., Klemp and Lilly (1980, p. 120). Here σ is the stability parameter defined in section 2 (for stable stratification is $\sigma = N^2$). For this figure the flow speed had been kept constant at 10 m s^{-1} and the Coriolis parameter was set to $f = 10^{-4}$ s^{-1}. Areas with l^2 less than zero have been shaded. Here vertically propagating waves do not form and there is no wave drag. In the upper left we find the gravity waves. This area is bounded for long horizontal wavelengths at the line $f^2 = k^2U^2$, and for smaller deviations from neutral stratification by the $\sigma = k^2U^2$.

The inner region of this area where $l^2 \approx \sigma/U^2$ is the region of hydrostatic mountain waves. Approaching the line $\sigma = k^2U^2$ we enter the nonhydrostatic regime, and approaching $f^2 = k^2U^2$ the rotation of the earth becomes important. The influence of stratification on the pressure drag is dealt with in section 5.

In the lower right corner of Fig. 4 we find inertial waves. This area is bounded for shorter horizontal wavelengths by line $f^2 = k^2U^2$ and for stronger stable stratification by $\sigma = k^2U^2$. These waves are vertically propagating for weakly stable, neutral, and unstable stratifications. We see that the possibility for wave drag

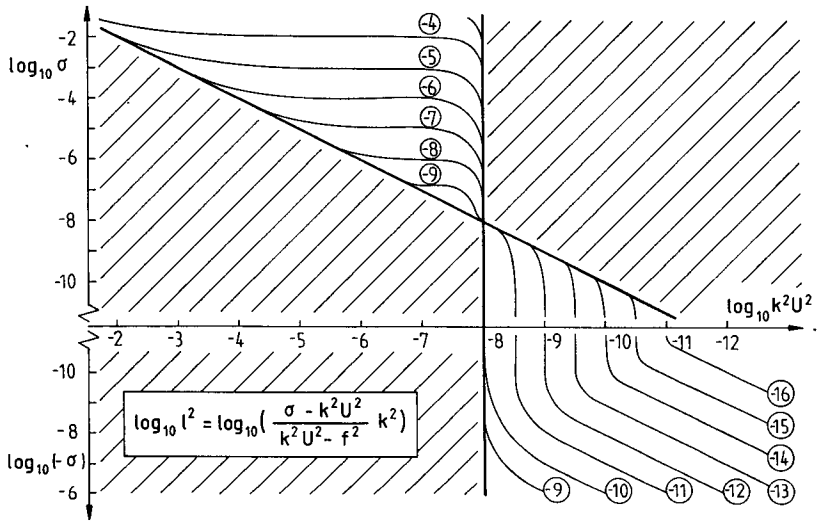

FIG. 4. Logarithm of the square of vertical wavenumber l as function of stratification ($\log\sigma$, σ negative for unstable conditions) and horizontal wavenumber k multiplied by wind speed U; $f = 10^{-4}$ s^{-1} and $U = 10$ m s^{-1}.

is not restricted to stable stratification. The breakdown of these waves under unstable conditions may initiate convection (He and Wu 1988, personal communication).

For unstable conditions the vertical wavenumber is approximately $l^2 = -\sigma k^2/f^2$ (σ negative). For neutral stratification the vertical wavenumber converges to $l^2 = k^4U^2/f^2$ for decreasing k, which means it is decreasing very rapidly. Here ($f^2 \gg k^2U^2$), we reach the regime of quasi-geostrophic motion where the pressure field is balanced by the Coriolis force and is changed by obstacles only in the manner that potential vorticity is conserved. This is the case that is dealt with in Smith (1979) who found a lift force on the mountain perpendicular to the incident flow but no drag force for f = const. Using Smith as an example, a drag force was possible only if the condition f = const. was relaxed and a β-plane was introduced. Now Rossby waves can form, which again produces a real drag force on the obstacle. This mountain torque is important in the global atmospheric angular momentum budget as a result of the long, north–south-oriented mountain ridges [see e.g., White (1949) and Lorenz (1967)]. These waves form for $U^2k^2 \leqslant U^2\beta^2/f^2 = 10^{-12}$ s^{-2} with $\beta = 10^{-11}$ m^{-1} s^{-1}.

Rossby waves are far outside the scope of the present numerical mesoscale model. In the right half of Fig. 3 we see just the beginning of the inertial wave regime where U^2k^2 is some 10^{-7}. The broken lines for different values of f in Fig. 3 show that the rise in drag with increasing Reynolds number really depends on the Coriolis parameter. The increase of the irrotational drag is proportional to $\mathrm{Re}_t^{-0.65}$.

Comparing the numerical results with (22) shows that the first integral with nondimensional quantities is of the order of 10 (as already found in section 4.1) and the second one is of the order of 1. The increase of the irrotational drag proportional to $\mathrm{Re}_t^{-0.65}$ corresponds nearly exactly to $\mathrm{Re}_t^{2/3}$ in (22), and the increase of the drag with Ro_o^{-1} can also be found from the numerical simulations presented in Fig. 3.

Thus the numerical results prove the functional dependencies of the drag on $\mathrm{Re}_t^{-2/3}$ and Ro_o^{-1}, as found from scaling considerations in section 2, to be right. Merely the viscous form drag comes out one order of magnitude larger than expected from the scale analysis. We think that the main reason for this is that a value too low for ν_t has been assumed and that the deformation of the velocity field takes place on a shorter length scale than L (this was input in (5) when we derived the turbulent velocity scale in section 2).

Also, the influence of the surface roughness can be studied from Fig. 3. For small roughness (surface Rossby number greater than about $5 \cdot 10^5$) the curves in the plot are nearly indistinguishable. For greater roughness the drag is increasing. This separation of smooth and rough obstacles is the same as for the drag coefficient for smooth and rough plates in the figures by Nikuradse and Prandtl.

Businger (1973) in reviewing Nikuradse's work gives the following values for smooth and rough surfaces of the parameter u_*z_0/ν (this can be regarded as the Reynolds number of the smallest eddies in the flow): the surface is smooth for $u_*z_0/\nu < 0.13$ and is completely rough for $u_*z_0/\nu > 2.5$. This ratio compares a viscous length scale at the surfae ν/u_* with the surface roughness z_0.

In our case we have to compare the turbulent length scale $\nu_t/u_{*\mathrm{eff}}$ ($u_{*\mathrm{eff}} = (u_*^2 + W_D/\rho)^{1/2}$) with the surface roughness

$$\frac{u_{*\mathrm{eff}}z_0}{\nu_t}. \tag{24}$$

Taking $u_{*\mathrm{eff}} \approx 0.5$ m s^{-1} and $\nu_t = 5$ m^2 s^{-1} we have smooth obstacles for $u_{*\mathrm{eff}}z_0/\nu_t < 10^{-2}$ and completely rough obstacles for $u_{*\mathrm{eff}}z_0/\nu_t > 10^{-1}$.

The only separation between the curves for smooth obstacles occurs in the vicinity of the drag minimum. This minimum is shifted to greater Reynolds numbers (i.e., smaller obstacle Rossby numbers) for smaller surface roughness. This means that the onset of the formation of inertial waves is slightly dependent on surface roughness. This was already deduced from Fig. 2 where the separating line between the subregion A1 and B1 was not exactly vertical. The smooth obstacles correspond to the subregions A1 and B1 in Fig. 2, the rough obstacles to A2 and B2.

The dependence of the form drag on the surface roughness, in the manner shown in Figs. 2 and 3, leads to the conclusion that the form drag can be partitioned into two parts: a part due to the viscosity of the air and a part due to the production of additional turbulence in the vicinity of the obstacles. The first (called viscous form drag) is independent of the surface Rossby number, the latter (called turbulent form drag) is nearly independent of the turbulent Reynolds number and is only present for rough obstacles.

5. Dependence of the drag on the stratification

The most prominent feature of nonneutral stratification, the wave drag with stable stratification, will not be discussed here. Our main focus is on form drag, with some consideration given to the influence of the hydrostatic contribution to the drag. Again as in section 4, we will see that turbulent viscosity of air will play an important role in form drag.

The main parameter determining the drag coefficient $C_W^{(2)}$, except the slope, will be the nondimensional stability parameter $\sigma^* = \sigma L^2/u_g^2$. For stable conditions σ^* is identical to Fr^2. For $\sigma^* < 0$ the stratification is unstable. For $0 < \sigma^* < \pi^2$ the stratification is stable but no vertically propagating waves are excited. For

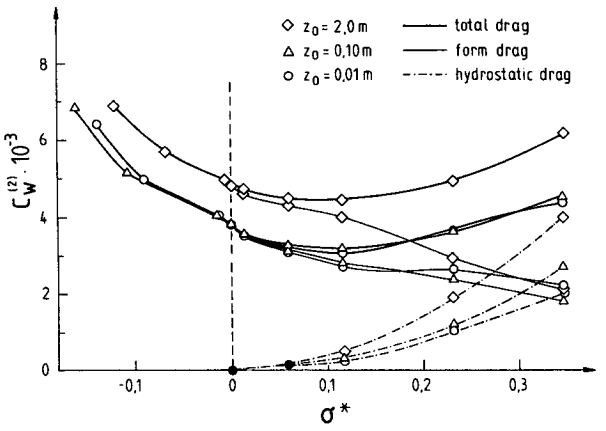

FIG. 5. Drag coefficient $C_W^{(2)}$ for slope $H/L = 0.1$ and $\mathrm{Ro}_o = 1.7 \cdot 10^2$ as function of the stability parameter σ^*. The plot is valid for different surface Rossby numbers (open symbols for different roughness lengths, full circles indicate that more than two symbols fall together). Thick curves show total pressure drag, thin curves viscous plus turbulent form drag, and dashed–dotted curves the hydrostatic part of the drag.

$\sigma^* > \pi^2$ waves are excited and the wave drag becomes important. Here, we will consider only $\sigma^* \ll \pi^2$.

Because form drag comes from turbulent viscosity of the air and turbulence production in the vicinity of the obstacle a clear dependence on stratification can be expected. Under stable stratification turbulence is suppressed and thus form drag should be lowered; under unstable conditions turbulence is enhanced and form drag should be increased compared to neutral stratification.

Figure 5 shows $C_W^{(2)}$ from (12) for an obstacle 50 m high and with slope $H/L = 0.1$ plotted against the stability parameter σ^*. The range of the stability parameter is restricted to values where gravity wave drag does not occur. For $\sigma^* > 0$ the stability parameter has been determined from the mean vertical temperature gradient, which is constant for the whole model domain (it is therefore an external parameter). For $\sigma^* < 0$ the local temperature gradient between 15 m and 160 m in the undisturbed flow upstream of the obstacle has been taken (see section 3 how the model has been initialized for the different stratifications). Three different measures for the pressure drag are plotted in Fig. 5—the total pressure drag calculated from the surface pressure distribution, viscous plus turbulent form drag (stable stratification only), and hydrostatic drag.

The following features are obvious from these results:

1) Minimum total pressure drag is found for slightly stable stratifications. This is because form drag is decreasing more rapidly with σ^* than the hydrostatic drag is increasing for weakly stable situations.

2) Again, as in Fig. 3, a distinction between smooth and rough obstacles can be made. For $z_0 \leq 0.1$ m the obstacles are smooth and the drag does not depend on surface roughness. For $z_0 \geq 2$ m the obstacles are rough at least for unstable and netural conditions.

3) For stable stratification the difference in the form drag between rough and smooth obstacles is vanishing with increasing stability. This means that the production of additional turbulence in the vicinity of the obstacles is suppressed.

4) The turbulent viscosity of the air (expressed by the exchange coefficient for momentum) is changing with stratification. Therefore the variation of σ^* in Fig. 5 can be seen as a variation of the turbulent Reynolds number because u_g and L had been kept constant. As the form drag increases with increasing turbulent viscosity (more unstable) we again have as in Fig. 3 an inverse proportionality between drag and turbulent Reynolds number.

Taking the variation of the exchange coefficient for momentum with stratification at about 160 m above ground from the numerical model and using it as a measure for the variation of the turbulent viscosity and thus for the variation of Re_t with stability, we find that $C_W^{(2)}$ for small deviations from neutral conditions is roughly proportional to $\mathrm{Re}_t^{-0.5}$, which is quite close to the value found for neutral stratification ($\mathrm{Re}_t^{-0.65}$).

We can describe the pressure drag for small deviations from neutral conditions, no flow separation, and aerodynamically smooth obstacles by (21) if we allow for the variation of ν_t (and the Re_t) with stratification. This implies that we have $\mathrm{Re}_t = \mathrm{Re}_t(\sigma^*)$ for nonneutral stratification. Therefore we cannot express Ro_o in terms of Re_t as we have done in (22).

The results for the form drag for nonneutral stratification in Fig. 5 can be compared to experimental data from Graf et al. (1984). They collected data at a fixed platform in Lake Geneva using a 12-meter-high mast and computed from these measurements the drag coefficient for the surface of the lake at different stratifications. Their results are compared with our findings in Fig. 6.

The stability parameter z/L_* has been determined here in the same manner as Graf et al. (1984). For this procedure the Richardson number is formed

$$\mathrm{Ri} = \sigma \Big/ \left(\frac{\partial u}{\partial z}\right)^2 \tag{25}$$

where the velocity u is again taken at 15 m and 160 m height above ground in the undisturbed flow upstream of the obstacle. Then an empirical relation between Ri and z/L_* is used:

$$\frac{z}{L_*} = \begin{cases} 7.6\ \mathrm{Ri} & \text{for} \quad \mathrm{Ri} < 0 \\ 6.0\ \mathrm{Ri} & \text{for} \quad \mathrm{Ri} > 0. \end{cases} \tag{26}$$

It can be seen in Fig. 6 that form drag from gentle obstacles behaves similarly to the drag of a rough (lake)

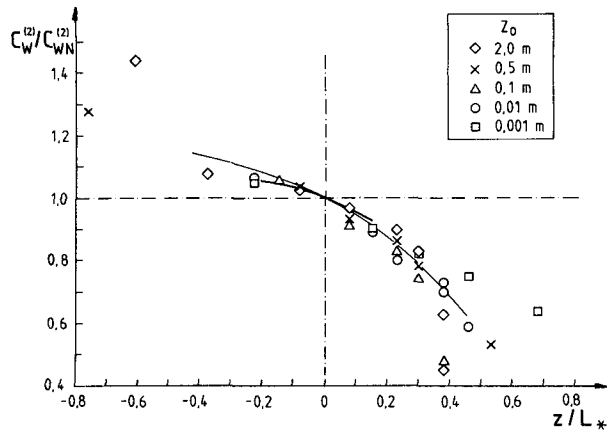

FIG. 6. Drag coefficient for form drag normalized with drag coefficient for form drag under neutral stability ($C_{WN}^{(2)}$) as function of z/L_*. Thin curve; fitted by eye through numerical results (different symbols); thick curve: experimental data from Graf et al. (1984).

surface under varying stratification. For larger deviations from neutral stability the scatter becomes considerable, probably due to the crude estimation of z/L_*.

6. Parameterization of pressure drag

In large-scale numerical models like operational forecast models and global climate models pressure drag on obstacles with horizontal scales less than a few 10^5 m is a subgridscale phenomenon which has to be parameterized. Drag due to Rossby waves, quasi-geostrophic lift forces, and in regional models ($\Delta x \approx 10^5$ m), inertial waves, can be resolved. Therefore, subgridscale processes that have to be dealt with are both parts of the form drag, the wave drag due to gravity waves, and the hydrostatic drag due to the blockage of colder air masses.

One possibility for including such subgridscale effects is to consider them as an additional surface roughness. Attempts to parameterize subgridscale drag in the same way as friction have been made by Fielder and Panofsky (1972), Kustas and Brutsaert (1986), and others who computed an effective roughness length under neutral to unstable conditions from aircraft and radiosonde data.

In E87 the Rossby number similarity theory has been used to compute an effective roughness length from numerical model output for neutral stratification. We want to investigate now if this concept can be extended to nonneutral stratification.

The resistance law (Blackadar and Tennekes 1968)

$$\ln \mathrm{Ro} = A - \ln C_D + \left(\frac{\kappa^2}{C_D{}^2} - B^2\right)^{1/2} \qquad (27)$$

with the surface Rossby number

$$\mathrm{Ro} = \mathrm{Ro}_s = \frac{v_g}{fz_0} \qquad (28)$$

and the geostrophic drag coefficient

$$C_D = \frac{u_*}{|v_g|} \qquad (29)$$

contain two stability-dependent parameters A and B. The dependence of A and B on the stability parameter $\mu = \delta/L_*$ (L_* Monin–Obukhov length) is known from experimental and theoretical studies. Using (27) (Fig. 7) shows the drag coefficient C_D as a function of the surface Rossby number ($\mathrm{Ro} = \mathrm{Ro}_s$) for different stratifications μ. The values for $A(\mu)$ and $B(\mu)$ have been taken from Fiedler (1972). Figure 7 is an extension of a similar figure from Wippermann (1972) to smaller surface Rossby numbers which ended at $\mathrm{Ro} = 10^5$. This extension has been done to include effective roughness length greater than about 1 m in the figure ($f = 1 \times 10^4\ \mathrm{s}^{-1}$ and $v_g = 8.5\ \mathrm{m\ s}^{-1}$ have been used to compute the scale on the left ordinate). The curve labeled $\mu = 0$ has been used to determine the effective roughness length in E87 from an effective drag coefficient

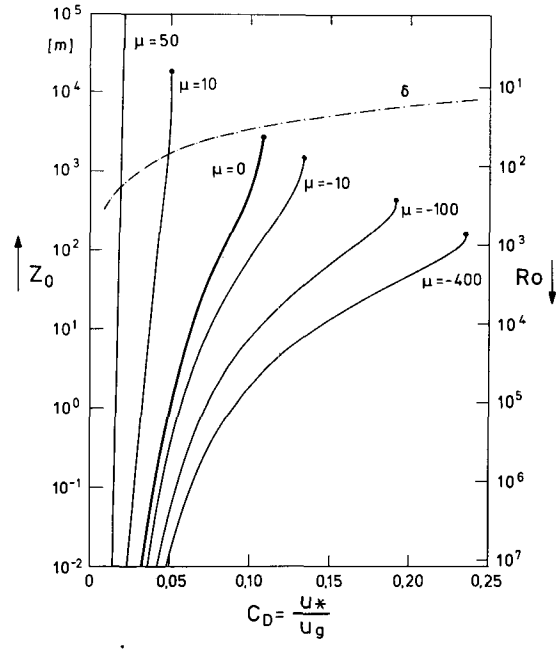

FIG. 7. Surface Rossby number (effective roughness length) as function of geostrophic drag coefficient C_D and stratification $\mu = \delta/L_*$ (L_* Monin–Obukhov length). The dashed-dotted line indicates the height of the boundary layer for neutral stratification for different values of C_D. $u_g = 8.5\ \mathrm{m\ s}^{-1}$.

$$C_{D\text{eff}} = \frac{[u_*^2 + (W_D/\rho)]^{1/2}}{|v_g|} \tag{30}$$

with W_D from (1).

The possible effective roughness lengths that can be computed from effective drag coefficients using (27) are restricted for two reasons. First, for mathematical reasons the curves end at the indicated positions because the square root in (27) becomes imaginary. However, second, the determination of a roughness length is only meaningful for a logarithmic wind profile. This logarithmic wind profile normally extends between about $10 \cdot z_0$ and about $1/10 \cdot \delta$. So $z_{0\text{eff}}$ must be smaller than about $1/100 \cdot \delta$ to allow for a logarithmic profile (see also Fig. 7). Therefore $z_{0\text{eff}}$ cannot be larger than 20 to 30 m. This is equivalent to surface Rossby numbers not much smaller than 10^4. This is obvious as the resistance law is valid only in the asymptotic limit of large Ro_s. From this consideration a value given by Thompson (1978) is questionable. He found from measurements over complex terrain of wind profiles for neutral stratification an effective roughness length of about 35 m. Presumably his winds were not in a dynamic equilibrium with the surface and the topography.

But another fact becomes clear from Fig. 7. For stable stratification no meaningful effective roughness lengths can be determined from (27) using effective drag coefficients from (30), because the drag coefficient is nearly independent of the Rossby number and therefore of the roughness length too. On the other hand, as seen from the previous section, an effective drag coefficient would increase rather rapidly for stable stratification once hydrostatic effects and gravity waves become important.

Two reasons are responsible for the failure of (27). First, the Rossby number similarity theory has been developed for horizontal homogeneity where no hydrostatic drag or wave drag can evolve. Second, the influence of obstacles under stable stratification are not restricted to the boundary layer when gravity waves are excited. Finally, momentum is extracted from layers far above the boundary layer. Such a process obviously cannot be described by a boundary layer theory.

From the aforementioned it is clear that the total pressure drag under stable stratification cannot be parameterized by an effective roughness length. Instead, the pressure drag in this case can be expressed in terms of an effective drag coefficient.

One part of the pressure drag under stable stratification that can be parameterized using the Rossby number similarity theory still remains—the viscous form drag that is due to the viscosity of the air passing over the obstacle. As seen in Fig. 5 this part of the drag is rapidly decreasing when the stratification becomes more stable. The effective drag coefficient due to this part of the drag entering (27) is converging against the drag coefficient over flat terrain and thus the effective roughness length remains within reasonable values.

For unstable stratification, only form drag exits (at least for length scales shorter than U/f) and the Rossby number similarity theory remains applicable. Here, the form drag is larger than under neutral stratification and from Fig. 7 it is clear that we need a larger increase in the effective drag coefficient to reach the same effective roughness length than under neutral conditions, if we assume that the roughness length itself is independent of the stratification.

The introduction of an effective roughness length is only meaningful for an ensemble of obstacles, not for an isolated obstacle. The parameter study in the two previous sections are only the first step towards a complete parameterization of pressure drag. They were mainly designed to clarify the nature of the different parts of the drag.

The findings from sections 4 and 5 can be applied to $C_W^{(2)}$. Assuming that the different parameters are independent of each other we will have, for the form drag without flow separation for an isolated obstacle (mountain),

$$C_W^{(2)} = \left(\frac{H}{L}\right)^2 \cdot \left(\frac{6.082}{\text{Re}_t^{2/3}} \cdot 10 + \frac{1}{\text{Ro}_o} \cdot 1\right) + f_2(\text{Ro}_s). \tag{31}$$

The second term (f_2) is a correction of the turbulent form drag on rough obstacles. Both terms together are $f^{(2)}$ from (12) for $\text{Fr}_h = 0$ and Ro_p approaching infinity. The dependence on σ^* is contained in $\text{Re}_t(\sigma^*)$.

7. Conclusions

Obstacles in the atmospheric boundary layer produce a pressure drag on the atmosphere. It can be divided into drag and lift forces. Including viscosity of the air, surface roughness, stratification, and rotation, drag can be broken into six parts (see also Fig. 8, $\text{Ro}_c \approx 5 \times 10^5$):

1) Form drag due to the turbulent viscosity of the air (viscous form drag).

2) Form drag due to the production of additional subgridscale turbulence in the vicinity of rough obstacles (turbulent form drag) (also, for steeper obstacles the production of gridscale turbulence in form of separation bubbles in the lee of the obstacles).

3) Wave drag due to gravity waves for stable stratification.

4) Wave drag due to inertial waves.

5) Wave drag due to Rossby waves.

6) Hydrostatic drag due to the blockage of colder air masses.

Wave drag due to Rossby waves is outside the scope of this paper. It forms part of the global angular mo-

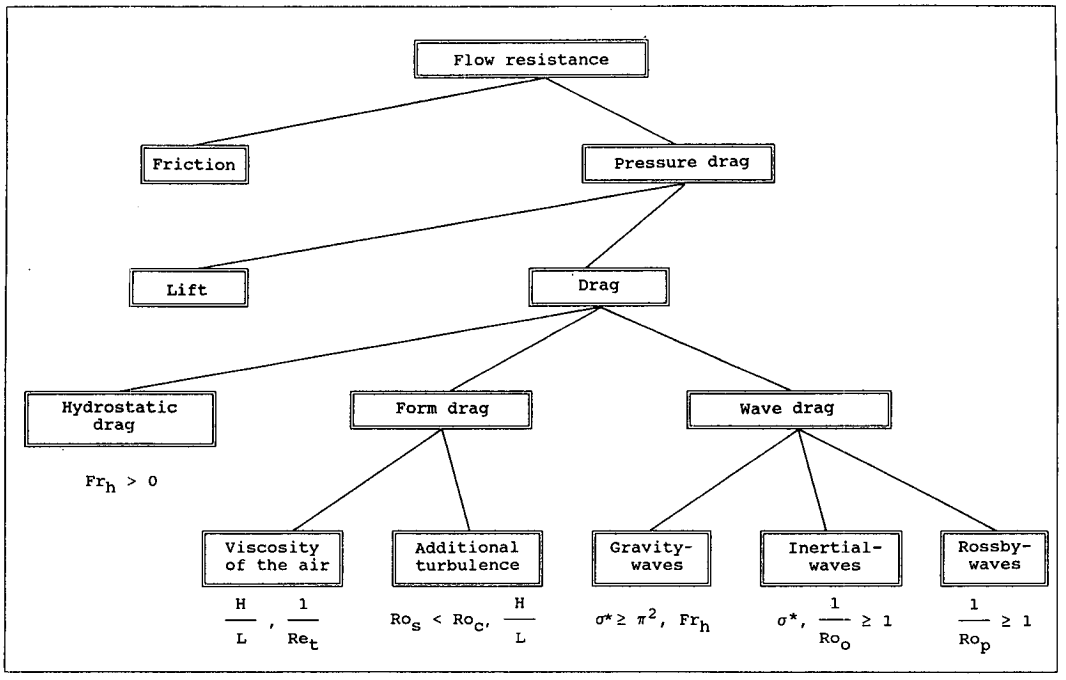

FIG. 8. Schematic decomposition of flow resistance. Below the different parts of the drag the main scaling parameters are listed ($Ro_c \approx 5 \cdot 10^5$).

mentum budget and is resolved in larger-scale models; therefore a parameterization is not necessary.

Wave drag due to inertial waves is a feature mainly present under neutral and unstable stratifications but is restricted to large horizontal wavelengths of the obstacles (L at least 10–100 km). This scale can partly be resolved by regional models ($\Delta x \approx$ 50–100 km). The onset of inertial wave drag was found in the present model at about $Ro_o = 30$. For $Ro_o \geq 10$ inertial wave drag is included in the parameterization for the drag of a single obstacle (31).

Wave drag due to gravity waves is not addressed here.

The two components of form drag have been the main scope of this paper. As shown in E87 the main parameter scaling this drag is the square of the slope H/L of the obstacle. The present paper deals with the additional parameters that influence the drag, too. Keeping the slope constant, these are surface roughness, stratification, viscosity of the air, and length of the obstacle. Normalizing the pressure drag with the kinetic energy of the geostrophic flow introduces another parameter, the height of the boundary layer δ. As the scaling velocity has to be taken from a height above ground, which is a function of the length scale of the obstacle (Jackson and Hunt (1975)), L/δ is an important parameter for the drag.

Removing the effects of H/L and L/δ the following statements can be made about the form drag of this study:

1) The turbulent form drag due to additional production of subgridscale turbulence in the vicinity of the obstacle (mainly on the lee side) depends strongly on surface roughness. For small surface roughness the obstacle can be regarded as aerodynamically smooth and this part of the form drag vanishes. The remaining part of the form drag is independent of surface roughness and we have Rossby number similarity. Thus, this similarity theory can be extended from flat to complex terrain in the case of pure form drag for small surface roughness.

2) The viscous form drag is decreasing for increasing length scale L of the obstacle and for increasing stratification (from unstable to stable). The dependence of the viscous form drag on stratification can be compared to the variation of the surface drag coefficient $u_*/u(z)$ with stability from experimental data over a lake. This again shows that viscous form drag behaves like frictional drag.

3) For large Ro_o ($\geq$30) and fixed H/L (no flow separation) the form drag over an obstacle is similar to the frictional drag of a laminar flow over a rough plate if ν is substituted by ν_t and Re by Re_t. Form drag with flow separation is similar to turbulent flow over a rough plate with the above mentioned substitutions.

4) "Viscosity" here is the turbulent viscosity of the air, not molecular viscosity, because the latter should not depend on stratification. Furthermore, the Reynolds number formed with molecular viscosity is clearly beyond the critical value for the onset of turbulent mo-

tion. Finally, outside the thin laminar surface layer the present numerical model knows only the turbulent viscosity in terms of exchange coefficients computed from the turbulent closure for the Navier–Stokes equations. Thus we have the case of a similarity with respect to the usual Reynolds number (no dependence on the molecular viscosity) but no similarity with respect to the turbulent Reynolds number (dependence on the intensity of subgridscale turbulent motion).

5) This dependence of the viscous form drag should bring about the following possibility: from a measurement of the pressure drag for an obstacle with known geometry, it should be possible to determine the turbulent viscosity of the air for different stratifications. Unfortunately, because pressure drag is one bulk value for the whole flow domain influenced by the obstacle, only a mean turbulent viscosity could be computed for the domain.

6) The form drag computed from the numerical model depends on the turbulent closure of the model. Because the production of additional turbulence in the lee with steeper obstacles is more sensible to the turbulent closure than the mean viscosity of the air (for flat obstacles this should not differ very much from the values for homogeneous terrain), the viscous form drag should not depend decisively on the turbulent closure of the numerical model.

7) The form drag calculated from the numerical model results shows the dependence on the nondimensional parameters H/L, Re_t, and σ^* as expected from the scaling of the equation of motion in section 2. The exact magnitude of the drag gives hints to improve this scaling procedure. The coincidence of the numerical results with the scaling leads to the parameterization of the form drag (and inertial wave drag) for one isolated obstacle in (31).

8) The measuring of pressure drag for known stratification, roughness length, and geometry of the obstacle is a means by which to check the parameterization of turbulence in a numerical model. As already mentioned in the Introduction no experimental data on the different parts of the drag for mesoscale obstacles are known to the author.

The hydrostatic drag only appears under stable stratification. It is a function of Fr_h rather than of Fr.

Parameterization of pressure drag in larger scale models (in the same manner as surface friction) is possible only for form drag because only this part of the drag can be compared to the drag over homogeneous terrain. All other parts of the drag have no corresponding mechanisms in the homogeneous boundary layer. They have to be described by additional terms in the model equations that are not present in the equations for the homogenous boundary layer.

Future work will extend the numerical studies to ensembles of obstacles in order to complete the task of parameterization. A first step towards this aim was presented for a very limited range of parameters in Emeis (1987).

Acknowledgments. This study has been funded by the Deutsche Forschungsgemeinschaft. It is part of work done in the SFB 210 Strömungsmechanische Bemessungsgrundlagen für Bauwerke at Karlsruhe University. I thank Professor Fiedler for initiating and encouraging this work and my colleagues at the Institut für Meteorologie und Klimaforschung for helpful discussions. I also like to thank the reviewers whose comments helped to clarify the structure of this paper. Thanks are last but not least to Mrs. Urbanek for drawing the figures.

APPENDIX

Symbols

$A(\mu)$	stability dependent constant
$B(\mu)$	stability dependent constant
C_D	drag coefficient for surface friction $u_*/\lvert v_g\rvert$
C_W	drag coefficient for pressure drag, see (8)
Fr	Froude number NL/u_g
Fr_h	Froude Number NH/u_g
H	maximum height of obstacle, see (10)
L	half of width of sinusoidal obstacle, see (10)
L_*	Monin–Obukhov length
N	Brunt–Väisälä frequency
Re	Reynolds number u_gL/ν
Re_t	turbulent Reynolds number u_gL/ν_t
Ro_o	obstacle Rossby number u_g/fL
Ro_p	planetary Rossby number $u_g/\beta L^2$
Ro_s	=Ro, surface Rossby number u_g/fz_0
U	velocity scale
W_D	pressure drag normalized with length of sloped terrain, see (1)
f	Coriolis parameter
$h(x)$	topography, see (10)
k	horizontal wavenumber, see (23)
l	vertical wavenumber, see (23)
p	pressure, deviation from a basic state without obstacle
β	north–south gradient of Coriolis parameter
δ	height of boundary layer $\kappa u_*/f$
ϵ	dissipation
κ	van Kármán's constant (=0.4)
μ	stability parameter δ/L_*
ν	molecular viscosity of air
ν_t	turbulent viscosity of air
σ	stability parameter $g/\theta \cdot \partial\theta/\partial z$, $=N^2$ for stable conditions
σ^*	nondimensional stability parameter = Fr^2 for stable conditions

REFERENCES

Blackadar, A. K., and H. Tennekes, 1968: Asymptotic similarity in neutral barotropic planetary boundary layers. *J. Atmos. Sci.*, **25**, 1015–1020.

Businger, J. A., 1973: Turbulent transfer in the atmospheric surface layer. *Workshop on Micrometeorology,* D. A. Haugen, Ed., American Meteorological Society, 67–100.

Davies, H. C., and P. D. Phillips, 1985: Mountain drag along the Gotthard section during ALPEX. *J. Atmos. Sci.,* **42,** 2093–2109.

Dorwarth, G., 1986: Numerische Berechnung des Druckwiderstands typischer Geländeformen. *Ber. Inst. Meteorol. Klimaf. Karlsruhe, No. 6,* 152+XII pp. (Available from: Institute für Meteorologie und Klimaforschung, Kaiserstr. 12, D-7500 Karlsruhe 1, Fed. Rep. of Germany.)

Emeis, S., 1987: Pressure drag and effective roughness length with neutral stratification. *Bound.-Lay. Meteor.,* **39,** 379–401.

——, 1990: Surface pressure distribution and pressure drag on mountains. Submitted to: *Meteorol. Atmosph. Phys.* (Special issue 'International Conference on Mountain Meteorology and ALPEX'.)

Fiedler, F., 1972: Der Einfluß der Baroklinität auf das Widerstandsgesetz in einer diabatischen Ekman Schicht. *Beitr. Phys. Atmosph.,* **45,** 164–173 (in English).

——, and H. A. Panofsky, 1972: The geostrophic drag coefficient and the "Effective Roughness Length." *Quart. J. Roy. Meteor. Soc.,* **98,** 213–220.

Graf, W. H., N. Merzi and C. Perrinjaquet, 1984: Aerodynamic drag: Measured at a Nearshore Platform on Lake of Geneva. *Arch. Met. Geoph. Bioklim.,* **A33,** 151–173.

Hafner, T. A., 1987: Experimentelle Untersuchungen zum Druckwiderstand der Alpen. *Ber. Inst. Meteorol. Klimaf. Karlsruhe, No. 9,* 217 pp. (Available from: Institut für Meteorologie und Klimaforschung, Kaiserstr. 12, D-7500 Karlsruhe 1, Fed. Rep. of Germany.)

——, and R. B. Smith, 1985: Pressure drag on the European Alps in relation to synoptic events. *J. Atmos. Sci.,* **42,** 562–575.

He, H., and C. Wu, 1988: Personal communication.

Jackson P. S., and J. C. R. Hunt, 1975: Turbulent wind flow over a low hill. *Quart J. Roy. Meteor. Soc.,* **101,** 929–955.

Klemp, J. B., and D. K. Lilly, 1980: Mountain waves and momentum flux. In: *Orographic Effects in Planetary Flows. GARP Publ. Ser.,* **23,** WMO, 115–141.

Kustas, W. P., and W. Brutsaert, 1986: Wind profile constants in a neutral atmospheric boundary layer over complex terrain. *Bound.-Layer Meteorol.,* **34,** 35–54.

Lorenz, E. N., 1967: The nature and theory of the general circulation of the atmosphere. WMO No. 218, TP 115, 161 pp.

Mellor, G. L., and T. Yamada, 1982: Development of a turbulent closure model for geophysical fluid problems. *Rev. Geophys. Space Phys.,* **20,** 851–875.

Prandtl, L., et al, 1984: Führer durch die Stömungslehre. Vieweg, Braunschweig, 622 pp.

Shao, Y., and M. Hantel, 1986: Subsynoptic vertical momentum flux in the atmosphere over Europe. *Bonner Meteorol. Abhandl.,* 33, 159 pp. (Available from : Meteorologisches Institut, Auf dem Hügel 20, D-5300 Bonn 1, Fed. Rep. of Germany.)

Smith, R. B., 1978: A measurement of mountain drag. *J. Atmos. Sci.,* **35,** 1644–1654.

——, 1979: Some aspects of the quasi-geostrophic flow over mountains. *J. Atmos. Sci.,* **36,** 2385–2393.

——, 1989: Mountain-induced stagnation points in hydrostatic flow. *Tellus,* **41A,** 270–274.

Sykes, R. I., 1980: An asymptotic theory of incompressible turbulent boundary layer flow over a small hump. *J. Fluid. Mech.,* **101,** 647–670.

Tennekes, H., 1973: Similarity laws and scale relations in planetary boundary layers. *Workshop on Micrometeorology,* D. A. Haugen, Ed., American Meteorological Society, 177–216.

Thompson, R. S., 1978: Note on aerodynamic roughness length for complex terrain. *J. Appl. Meteor.,* **17,** 1402–1403.

White, R. M., 1949: The role of mountains in the angular momentum balance of the atmosphere. *J. Meteor.,* **6,** 353–355.

Wippermann, F., 1972: Empirische Formeln für die universellen Funktionen $M(\mu)$ und $N(\mu)$ im Widerstandsgesetz einer barotropen und diabatischen planetarischen Grenzschicht. *Beitr. Phys. Atmosph.,* **45,** 305–311 (in English).